Correlating Oxidation State and Surface Area to Activity from *Operando* Studies of Copper CO Electroreduction Catalysts in a Gas-Fed Device

Soo Hong Lee,[#] Ian Sullivan,[#] David M. Larson, Guiji Liu, Francesca M. Toma, Chengxiang Xiang,* and Walter S. Drisdell*

ACCESS | Metrics & More | Article Recommendations | SI Supporting Information

ABSTRACT: The rational design of high-performance electrocatalysts requires a detailed understanding of dynamic changes in catalyst properties, including oxidation states, surface area, and morphology under realistic working conditions. Oxide-derived Cu catalysts exhibit a remarkable selectivity toward multicarbon products for the electrochemical CO reduction reaction (CORR), but the exact role of the oxide remains elusive for explaining the performance enhancements. Here, we used *operando* X-ray absorption spectroscopy (XAS) coupled with simultaneous measurements of the catalyst activity and selectivity by gas chromatography (GC) to study the relationship between oxidation states of Cu-based catalysts and the activity for ethylene (C_2H_4) production in a CO gas-fed cell. By utilizing a custom-built XAS cell, oxidation states of Cu catalysts can be probed in device-relevant settings and under high current densities (>80 mA cm^{-2}) for the CORR. By employing an electrochemical oxidation process, we found that the Cu oxidation states and specific ion species do not correlate with C_2H_4 production. The difference in the CORR activity is also investigated in relation to electrochemical surface area (ECSA) changes. While the hydrogen evolution reaction (HER) activity is positively correlated to the ECSA changes, the increased C_2H_4 activity is not proportional to the ECSA. *Ex situ* characterization from microscopic techniques suggests that the changes in the C_2H_4 activity and selectivity may arise from a morphological transformation that evolves into a more active structure. These comprehensive results give rise to the development of a cell regeneration method that can restore the performance of the Cu catalyst without cell disassembly. Our study establishes a basis for the rational design of highly active electrocatalysts for broad-range reactions in a gas-fed device.

KEYWORDS: *operando X-ray absorption spectroscopy, electrochemical CO reduction, oxide-derived copper electrocatalyst, gas diffusion electrode, oxidation state*
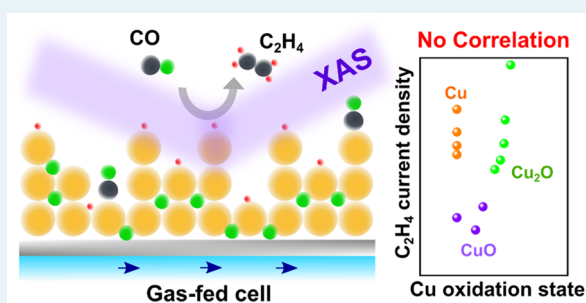
INTRODUCTION

The electrochemical carbon monoxide and carbon dioxide reduction reactions (CORRs and CO$_2$RRs, respectively) are promising strategies to convert waste emissions into valuable chemical feedstocks, such as synthesis gas, hydrocarbons, and oxygenates.[1−4] The CORR process is specifically interesting because it can be part of a tandem catalysis system, in which the first catalytic reaction converts CO$_2$ into CO, and the second catalytic reaction converts CO into higher-order reduction products such as ethanol or ethylene.[5,6] By leveraging the efficient and selective first two-electron, two-proton process from CO$_2$ to CO, analyses show that the optimal solar-to-fuel conversion efficiency of a tandem catalysis system was higher than that of the direct CO$_2$RR system at all cathodic overpotential and faradaic efficiency (FE) combinations.[7] In the CORR process, copper-based materials are the only electrocatalysts that can produce more reduced hydrocarbons and oxygenates due to the optimal Cu−CO binding

strength.[8,9] For lower activation overpotentials and increased FEs, Cu-based catalysts have been tuned via nanostructuring,[10] modifying the electrochemical surface area (ECSA),[11] or through the introduction of a second metal.[12,13] In particular, oxide-derived Cu (OD-Cu) prepared from the oxidative treatment of polycrystalline Cu resulted in high CO reduction selectivity toward multicarbon oxygenates at modest potentials.[14] Although the high CO reduction activity was correlated to surface sites that bind CO strongly,[15,16] the detailed mechanism for catalytic enhancement and surface structure during CORR remains elusive.
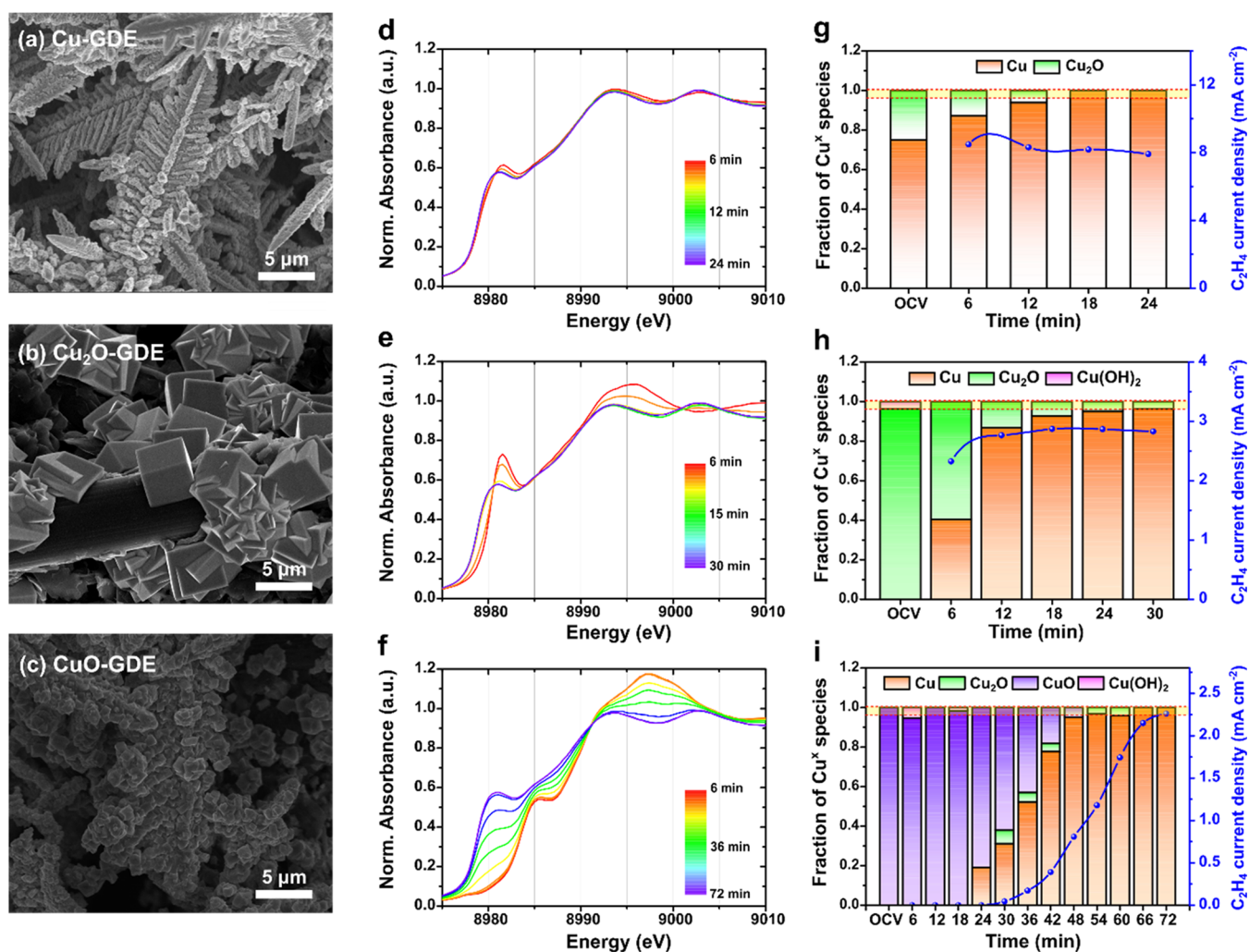
Figure 1. Catalyst structural characterization and *operando* XANES spectra during CORR. (a−c) SEM images of the as-synthesized Cu-GDE (a), Cu_2O-GDE (b), and CuO-GDE (c). (d−f) Temporal changes of Cu K-edge XANES spectra of Cu-GDE (d), Cu_2O-GDE (e), and CuO-GDE (f) acquired during the CORR at −2.2 V versus Ag/AgCl. (g−i) The calculated fraction of Cu oxidation states of Cu-GDE (g), Cu_2O-GDE (h), and CuO-GDE (i) from a LCF analysis with respect to the reaction time. GC measurements for the C_2H_4 partial current density (blue traces) were synchronized with XANES measurements and collected every 6 min. The yellow shaded region represents the estimated error range of up to 4% in the LCF analysis. The data shown in panels g, h, and i are derived from XANES spectra in panels d, e, and f, respectively.

To understand the origin of the superior catalytic activity of OD-Cu in comparison to polycrystalline Cu, previous studies focused on structural transformations during oxidation and subsequent *in situ* reduction.[17,18] This oxidation−reduction process increases the surface roughness, which can create high densities of grain-boundaries.[19] The grain-boundary surface terminations showed a selective increase in the CO_2RR activity but not for the parasitic hydrogen evolution reaction (HER).[20] This observation triggered a detailed mechanistic question of whether the activity enhancement comes from an increase in the number of active surface sites or an increase in the intrinsic activity of a specific active site. An extensive effort for investigating the active site has concentrated on detecting Cu+ and subsurface oxides while under operation, as theoretical calculations suggest that these species can improve the kinetics and thermodynamics of CO dimerization.[21] The presence of Cu+ and subsurface oxygen under highly reductive conditions was confirmed by microscopic and spectroscopic techniques,[22,23] but most of these studies did not run the CORR or CO_2RR, so it is unclear if catalytic environments during the measurements are relevant to the actual catalytic reaction. The

experiments also relied on *ex situ* or quasi *in situ* tools that cannot exclude the possible rapid reoxidation of OD-Cu before measurement.[24,25] Moreover, in many studies of the highly active Cu-based catalysts, the explanation for high performance depends on simple confirmation of Cu+ or oxygen content, with no proof of whether they are involved in the catalytic reaction or not. These uncertainties hinder the development of general relationships between the catalyst structure and activity.

In order to investigate oxidation states of Cu catalysts during the CORR, previous studies utilized *operando* XAS cells that are modified from an existing high-performance cell design.[26,27] These cells, however, typically operate at total current densities of up to 5 mA cm−2, much lower than the operating conditions for catalyst performance measurements, which can exceed 100 mA cm−2.[28] The *operando* conditions are not necessarily representative because the surface of the catalyst and local environments are known to be very sensitive to changes in the reaction rate and cell configurations.[29] The structural information obtained in such controlled conditions often ignores CO mass transport limitations and may not

represent the real oxidation states under practical operating conditions. Although the gas-diffusion layer (GDL)-based cell setup has been explored to overcome the mass transport limitations,[30] a careful evaluation of the CORR activity and selectivity in the modified *operando* cell is still needed to guarantee that the observed catalyst structure represents the real situation under operating conditions.[31,32] By considering these circumstances, we set our research goals as follows. First, investigating the direct relationship between oxidation states and the CORR performance using a well-configured *operando* XAS cell is required to understand the exact roles of oxide phases. Of particular interest is the oxidation state of a catalyst under high current densities without the depletion of CO molecules. Second, we set out to determine if dynamic changes in the catalyst surface area can influence C_{2+} selectivity and activity. Addressing these goals is required to formulate the general design principles for active CORR electrocatalysts.

Herein, we report a time-resolved *operando* study on the effect of oxidation states on the CORR performance by XAS and online GC, which allows for the simultaneous monitoring of the chemical valence state and product selectivity. We prepared three types of Cu catalysts with different oxidation states and introduced an electrochemical oxidation process, which enabled us to investigate the relationship between oxidation states and C−C coupling. By utilizing a modified gas-diffusion electrode (GDE) cell and an extensive fitting analysis, we demonstrated that the oxidation states of Cu catalysts during the CORR do not correlate with ethylene production under high reaction rates (>80 mA cm^{-2}). We also found that an increase in the number of active sites estimated by the electrochemical surface area (ECSA) was not proportional to the C_2H_4 yield. The post-mortem microscopic characterization indicated that the increased CORR performance may be due to morphological transformations during the electrochemical oxidation and its subsequent reduction that generate a more active Cu structure. On the basis of our findings, we applied this electrochemical oxidation process to restore both the activity and selectivity for C_2H_4 production and demonstrated continuous operation over 6 regeneration cycles.

RESULTS AND DISCUSSION

Synthesis and CORR Activity of Cu Catalysts in an *Operando* XAS Cell. To determine the relationship between oxidation states and the CORR performance, we carefully designed synthetic protocols to synthesize three catalysts with three different oxidation states of Cu. The crystalline structure and morphology of the three as-prepared Cu catalysts were confirmed by X-ray powder diffraction (XRD) and scanning electron microscopy (SEM). The XRD analysis indicated that Cu_2O-GDE and CuO-GDE show good agreement with characteristic Cu_2O and CuO peaks, respectively (Figure S1). The Cu-GDE not only had peaks that matched with metallic Cu but also had a small amount of Cu_2O due to the spontaneous oxidation in ambient air. In SEM images, both Cu-GDE and CuO-GDE show dendritic structures with sizes ranging 5−10 μm. Cu-GDE exhibited a sharper dendritic structure, while CuO-GDE exhibited more rounded tips (Figure 1a and 1c). The Cu_2O-GDE exhibited a cubic-shaped morphology with a size of less than 10 μm (Figure 1b).

For evaluating the electronic structure and oxidation states during the CORR, we used minimal modifications to an existing gas-fed cell, incorporating an X-ray transmissive window to accommodate *operando* XAS measurements (Figure

S2). The gas-fed cell is based on a hybrid catalyst-bonded membrane device that exhibited a total operating current density of up to 87 mA cm^{-2} at −2.0 V (vs Ag/AgCl; hereafter, all voltage is versus Ag/AgCl).[33] We first characterized the CORR activity and selectivity of the Cu-GDE in the *operando* XAS cell to verify the effects of cell modification on the catalyst performance. The total current density reached 80 mA cm^{-2} at −2.2 V, and its trend followed an exponential increase for the potential window of −1.6 V to −2.2 V, demonstrating sufficient CO mass transport over these potential ranges (Figure S3a and S3b). The FE for C_2H_4 and H_2 generation reached ∼11 and ∼79% at −2.2 V, respectively. (Figure S3c). Compared to the CORR performance in the original gas-fed cell, we found slight differences in the calculated FE for C_2H_4 selectivity (decreased from 18 to 11%) and for H_2 (increased from 51 to 79%) in the *operando* XAS cell. We ascribe these changes to the modified parts that may prevent the pressure buildup necessary to reduce water flooding (Figure S3d).[34] However, the *operando* XAS cell maintained similar total operating current densities (∼80 mA cm^{-2}) compared to the original cell, which allowed us to observe actual states of the catalyst structure under realistic operating conditions. During the *operando* XAS measurements, we were only able to detect gas products, including H_2 and C_2H_4, because space constraints in the beamline hutch did not allow us to sample the liquid products in real-time. The corresponding *operando* Cu K-edge XAS was obtained after a potential hold of 1 h. The XANES analysis shows that the Cu-GDE was a metallic Cu^0 phase after 1 h for all applied potentials except the potential at −1.6 V (Figure S4a and S4b). The EXAFS analysis indicates that all the samples have a prominent Cu−Cu scattering peak at 2.2 Å across a range of the applied potentials, which is indicative of the metallic Cu^0 phase. (Figure S4c). These data also demonstrated that performing *operando* XAS on Cu catalysts with different oxidation states enables us to systemically validate the contribution of oxidation states to the CORR catalytic activity of Cu-based materials in the gas-fed cell.

Probing Oxidation States of Cu Catalysts by *Operando* XAS. To investigate the Cu valence fraction in real-time during the CORR, we performed time-resolved XAS measurements of three Cu catalysts under the CORR operating conditions. We applied the potential of −2.2 V because it exhibited the highest FE for ethylene generation. During the *operando* XAS measurements, gas products were characterized by using on-line GC, and the GC and XAS measurements were synchronized such that both collected data every 6 min. (Figure S5). Other gaseous products such as methane and ethane exhibited negligible FEs during the bulk electrolysis (<0.2%). For the quantitative analysis of the Cu oxidation states, a linear combination fitting (LCF) was employed using a set of pure-valence references (Figure S6a).[35] Compared to the reference spectra, the observed XANES spectra presented a lower amplitude due to the overabsorption effect (Figure S6b). All the spectra were corrected for overabsorption by using a simple model (Table S1).[36] By using the synchronized measurements of GC and XAS with rigorous overabsorption correction and LCF, the *operando* XAS cell and analysis provided a useful platform to study the correlation between the catalyst oxidation states and catalytic performance for the CORR.

We tracked the change of XANES spectra for three Cu catalysts overtime under the fixed potential of −2.2 V (Figure
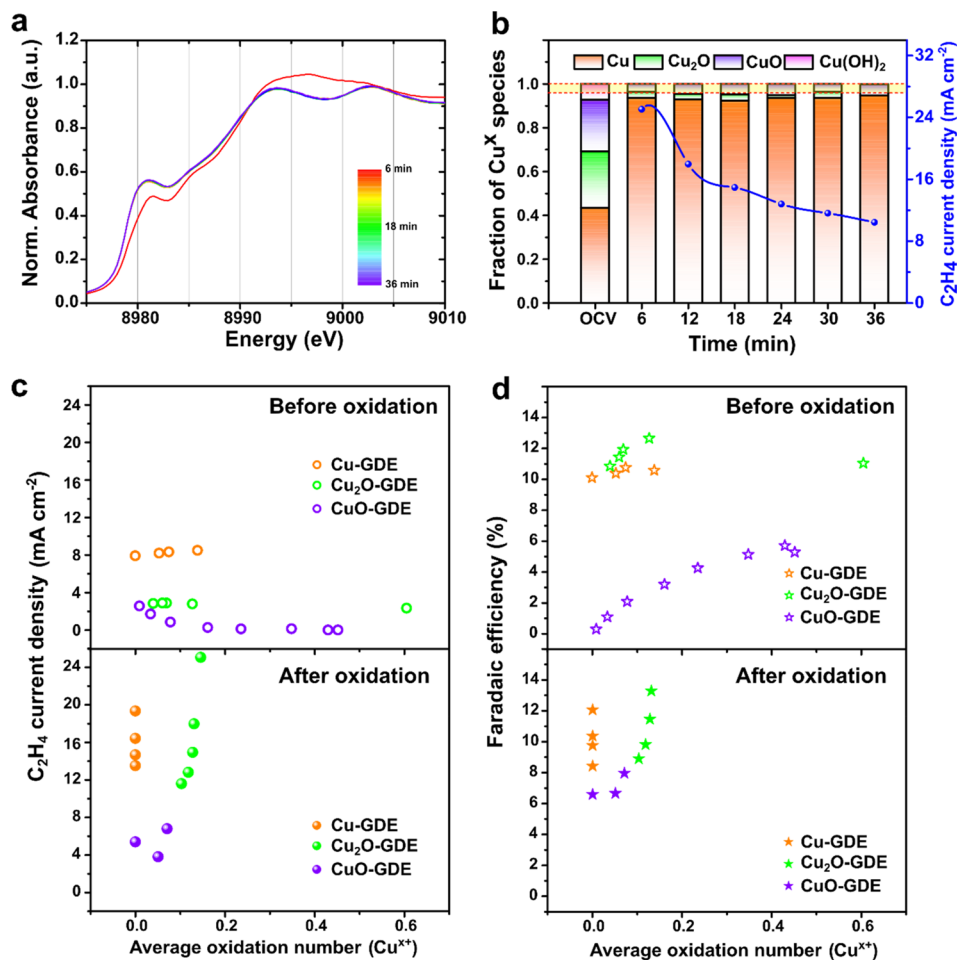
Figure 2. *Operando* XANES spectra during the CORR after electrochemical oxidation. (a) Temporal changes of Cu K-edge XANES spectra of Cu$_2$O-GDE after applying an anodic potential at 1.5 V versus Ag/AgCl for 5 min. After 6 min, every spectrum overlaps with each other. (b) The calculated fraction of the Cu oxidation states of Cu$_2$O-GDE after electrochemical oxidation. The yellow shaded region represents the estimated error range of up to 4% in the LCF analysis. (c) C$_2$H$_4$ partial current density and (d) faradaic efficiency of Cu catalysts as a function of Cu oxidation states before and after electrochemical oxidation. In terms of the CORR activity (C$_2$H$_4$ partial current density) and selectivity (faradaic efficiency), there is no correlation to the Cu oxidation states.

1d−1f). Repeated XANES spectra were collected until no further changes were observed. In the case of Cu-GDE and Cu$_2$O-GDE, the Cu$^+$ reduced to metallic Cu^0 within 20 min, and the C$_2$H$_4$ production was detected in the first GC measurement at 6 min (Figures 1g and 1h). Interestingly, CuO-GDE exhibited no detectable C$_2$H$_4$ product until the CuO phase began to reduce to the metallic Cu^0 phase at 24 min (Figure 1i). The trend of C$_2$H$_4$ partial current densities followed the evolution of the metallic Cu^0 phase and showed the maximum value after reducing all the residual oxide into Cu^0. This result suggests that CuO itself is inactive for the reduction reaction of CO molecules, and C−C coupling occurs only at the Cu^0 surface. Our observations were also in agreement with previously reported oxide-containing Cu catalysts that exhibited high C$_2$H$_4$ activity after a preactivation step.[30,37]

It is important to note that all the Cu catalysts reduced to metallic Cu^0 states during the CORR regardless of their initial oxidation states. Although the LCF analysis of Cu$_2$O-GDE shows ∼3.7% Cu$^+$ remaining in the Cu$_2$O-GDE after 30 min, this amount of residual oxides is within the error range of a LCF analysis. To estimate the error range in the LCF analysis, we introduced an empirical method by using normalized sum-

squares (NSS) as a best-fit criterion (Figure S7). In this respect, we conclude that the accuracy for the determination of Cu oxidation states via the LCF analysis is within 3−4%.

Correlation between Oxidation States and CORR Performance. Previous studies have claimed efficient C−C coupling during the CO$_2$RR from surface or subsurface Cu oxide species, which formed via an electrochemical oxidation process.[18,38,39] During the CO$_2$RR, the residual oxygen was mainly located in an amorphous 1−2 nm thick layer within the Cu subsurface.[23] Accordingly, we aimed in the next step to investigate the effects of surface oxide species on the CORR performance by applying an anodic potential to all the reduced Cu catalysts. The generation of the surface oxide structure was based on a previous study showing that copper oxide starts to grow at the surface at sufficiently high positive potentials in alkaline solutions.[40] A highly positive potential of 1.5 V was applied for 5 min to the Cu catalysts that had already converted into metallic Cu^0 states after the previous CORR. After the anodic oxidation, the XANES spectra show oxide features, and the LCF analysis reveals that copper oxides and hydroxides were formed in all Cu catalysts up to 60% (Figures 2 and S8). We then performed *operando* XANES measurements and evaluated the CORR performance simultaneously at
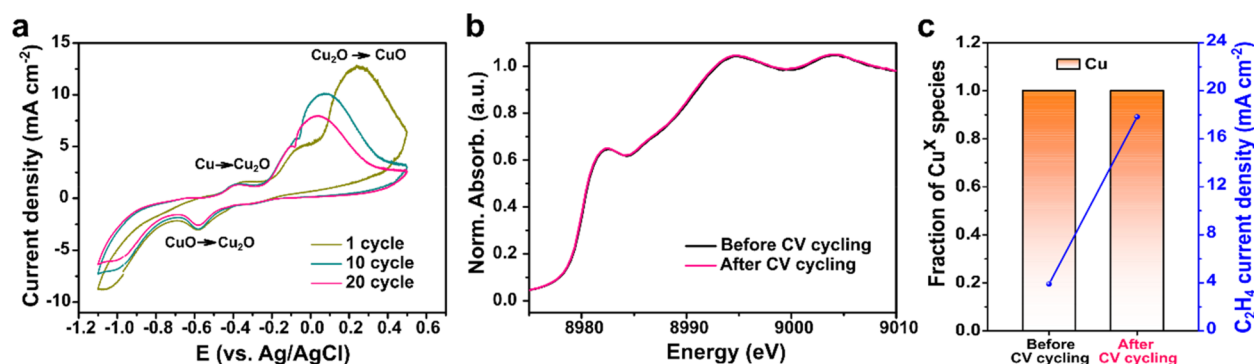
Figure 3. Electrochemical oxidation by using CV cycling. (a) CV curves of Cu-GDE recorded after electrolysis at -2.2 V versus Ag/AgCl. The anodic peaks related to the Cu oxidation into Cu(I) and Cu(II) and reduction are indicated. (b) *Operando* Cu K-edge XANES spectra of Cu-GDE before and after CV cycling. (c) The calculated fraction of Cu oxidation states before and after CV cycling and the corresponding C_2H_4 partial current densitie.

a fixed potential of -2.2 V. Unlike the previous CORR results before the anodic oxidation (Figure 1g–1i), most of the surface oxide and hydroxide species in all Cu catalysts were quickly reduced into metallic Cu^0 within the time resolution of the XANES measurements (<6 min) (Figures 2a and S8). The result suggests that the surface oxides are generally much easier to reduce than the initial oxides in the Cu catalysts. Moreover, similar features in the CORR selectivity and activity were observed through all the Cu catalysts. First, the total current densities of all the catalysts were increased after the anodic oxidation process, leading to significant enhancements of the partial current densities for both C_2H_4 and H_2 (Figure S9). In comparison to that of the initial Cu catalysts before the anodic oxidation treatment, $FE_{C_2H_4}$ increased and FE_{H_2} decreased in all Cu catalysts. Second, the enhanced partial current densities of C_2H_4 in all the Cu catalysts rapidly declined as the CORR proceeded.

Interestingly, the LCF analysis of Cu_2O- and CuO-GDE demonstrates that residual oxide species ($\sim5\%$) remained after further reaction time (Figures 2b and S8d). Although this amount of residual oxide is quite close to the error margins of the LCF analysis, its presence and persistence during the reaction have been regarded as the promoter for a C–C coupling.[24,41] We hypothesize that there could be an optimal oxidation state value or a linear correlation between the oxidation states and CORR performance if the residual oxide plays a role in the catalytic reaction. To verify this hypothesis and explore the relationship between oxidation states and CORR performance, we link the average oxidation number calculated from the LCF analysis and the CORR activity (vs C_2H_4 partial current density, Figure 2c) and selectivity (vs FE_{C2H4}, Figure 2d) before and after the anodic oxidation process. However, the oxidation states show no apparent correlation with the activity or selectivity. The contribution of each Cu ion species, including Cu^0, Cu^+, and Cu^{2+}, to the CORR activity and selectivity was also investigated, but no obvious trend was observed (Figure S10). Although hard XAS measurements at the Cu K-edge contains bulk-sensitive information and the LCF analysis cannot exclude the possible existence of residual oxides lower than 4%, this result is in contrast to the previous studies that utilized *in situ* XAS cells.[24,42] Our findings highlight the importance of a catalyst performance evaluation for an *operando* cell and the direct linkage between the observed XAS spectra and catalyst performance measured simultaneously.

We also tested the steady-state CV cycling method to regenerate the surface oxide on the Cu catalyst. This mild oxidative–reductive process in alkaline solutions has been used to induce step-wise reconstruction into a Cu(511) surface that catalyzes the conversion of CO molecules into ethanol.[43] The CV cycling method, with a cycling potential between -1.1 and 0.5 V for 20 cycles, was applied to the Cu-GDE that was already reduced into metallic Cu^0. The CV data indicate that Cu^+ was formed at -0.4 V, and Cu^{2+} was generated in the range of 0.05–0.25 V, leading to the formation of oxidized copper (Figure 3a).[40] This formed oxide was reduced again between -0.6 V and -1 V, as shown by the reductive wave in the CV. *Operando* XANES demonstrated that there was no change in the spectra before and after CV cycling (Figure 3b), and the LCF analysis confirmed that the two spectra indicate purely metallic Cu^0 states (Figure 3c). In contrast, the C_2H_4 partial current densities were increased about 4 times higher than those before the CV cycling (Figure 3c), consistent with the results from the oxidative treatment method. This result further supports our conclusion that the oxidation states of Cu catalysts fail to explain the difference in the catalytic activity and selectivity for the CORR in high current density operations >80 mA cm^{-2}.

Effects of Electrochemical Surface Area on CORR. The lack of a correlation between the oxidation state of Cu catalysts and CORR performance naturally points to another common factor, ECSA. It has been previously reported that the ECSA-normalized CORR activities of high and low surface area Cu are comparable, leading to the conclusion that both catalysts have a similar intrinsic activity.[44] The major difference in selectivity between these Cu catalysts was attributed to the lower intrinsic HER activity in high-ECSA catalysts due to local elevation of the pH from the rapid consumption of protons at high rates.[11,45] We investigated the role of the ECSA on CORR performance enhancement to understand whether the electrochemical oxidation can simply increase the number of active sites, or create new, more efficient active sites. The ECSAs of all the Cu catalysts were estimated by measuring the electrochemical double-layer capacitance (EDLC, Figure S11), which has been used to estimate a proxy for the wetted GDL electrode area in the gas-fed CO_2 electrolyzers.[46] Note that although the ECSA obtained by EDLC measurements could contain contributions from both the Cu catalyst and GDL, our deposition method (detailed in Experimental Section) is likely to cover the majority of the electrolyte-accessible portion of
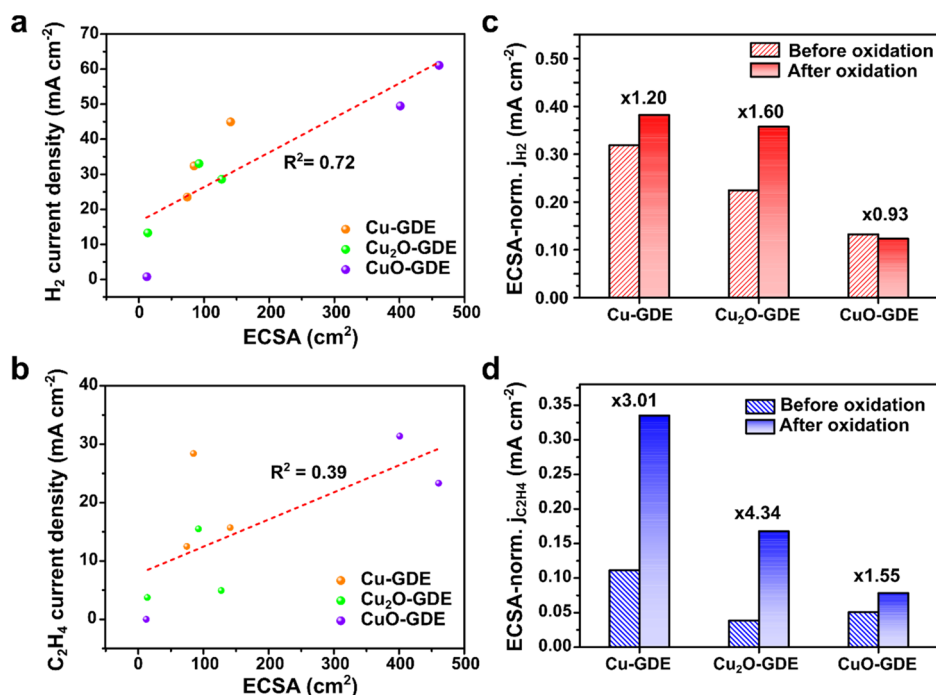
Figure 4. Relationship between the ECSA and activities for the HER and CORR. (a) H_2 and (b) C_2H_4 partial current densities of Cu catalysts as a function of the ECSA, estimated by EDLC. Normalized current densities by the ECSAs for each Cu catalyst for (c) H_2 and (d) C_2H_4 before and after electrochemical oxidation.

the GDL with the Cu catalyst. We therefore expect the EDLC measurements to provide a good approximation of the catalyst ECSA. The EDLC of the catalysts was measured at three periods before and after CORR and after anodic oxidation in the gas-fed cell (Table S2). All of the EDLCs of the Cu catalysts increased during the CORR and slightly decreased after anodic oxidation. The increase in EDLC during CORR could arise from the accelerating electrolyte ingress into the GDE. Such an increase in the EDLC is consistent with a previous report, where the passage of the faradaic current was found to lead to an increasing apparent hydrophilicity of a GDL over time, resulting in water flooding.[46] Also, we consistently observed salt crystallites on the catalyst layer in all the Cu catalysts (Figure S12). As salt crystallites form, they may draw water through the GDL via capillary forces, owing to their hygroscopic properties.[47]

On the basis of the above results, we measured partial current densities for C_2H_4 and H_2 at the same points where the ECSAs were obtained (Figure S13) and linked them to the ECSA of the Cu catalysts. We note that the total FEs for all of the Cu catalysts were less than unity because liquid products were measured from the anode side of the gas-fed cell where oxidation of some products can occur.[33] We observe that the ECSA value was positively correlated with the H_2 partial current density ($R^2 = 0.72$, Figure 4a), suggesting that the flooded electrolyte impeded the influx of CO gas to the catalyst surface and promoted HER. Such enhanced water flooding and higher rates of the HER were also observed in the *operando* XAS cell compared to that of the gas-fed cell (Figure S14). These results highlight that the characterization of the catalyst performance in the *operando* XAS cell is critical in order to guarantee the real operating condition of the CORR. The ECSA-normalized partial current densities for H_2 increased slightly or were similar before and after oxidation (Figure 4c), indicating that the intrinsic activity for the HER was not

affected by the anodic oxidation process. In contrast, there was no linear correlation between the ECSA and C_2H_4 partial current densities ($R^2 = 0.39$, Figure 4b), and the ECSA-normalized C_2H_4 current densities significantly increased after oxidation in all Cu catalysts (Figure 4d). Considering that wetted surfaces estimated by the EDLC values were slightly decreased after anodic oxidation, we explicitly exclude an increase in the number of active sites for the CORR from the reduction of the preoxidized catalyst as a cause of the increased activity in the gas-fed cell. Therefore, we conclude that electrochemical oxidation increases the C_2H_4 activity and selectivity by generating new, highly selective active sites for C−C coupling.

Morphological Transformation of Cu Catalysts during CORR. Our observations that neither the oxidation state nor the ECSA are correlated with the activity and selectivity suggest another catalyst property determining the CORR performance in gas-fed cells. Since Cu has a small cohesive energy and a high surface mobility, the surface of Cu undergoes severe reconstruction when exposed to gaseous CO[48] or under the CORR conditions.[49] In particular, the adsorption of CO into oxide-containing Cu catalysts invokes a surface reconstruction in the form of nanoclusters or fragmented structures that resulted in enhanced *n*-propanol production during the CORR.[30,37] This CO-induced surface reconstruction motivates us to investigate the relationship between morphological changes and the CORR performance of our Cu catalysts. To investigate the morphological evolution during CORR, we collected post-mortem SEM (Figures 5a−5c) and transmission electron microscopy (TEM) (Figures 5d−5f) images of Cu-GDE before and after electrolysis and electrochemical oxidation. The dendritic structure in the pristine Cu-GDE was composed of nanocubes with a size ranging 100−150 nm (Figure 5a) and a crystalline surface layer (Figure 5d). The fast Fourier transform (FFT) pattern of the
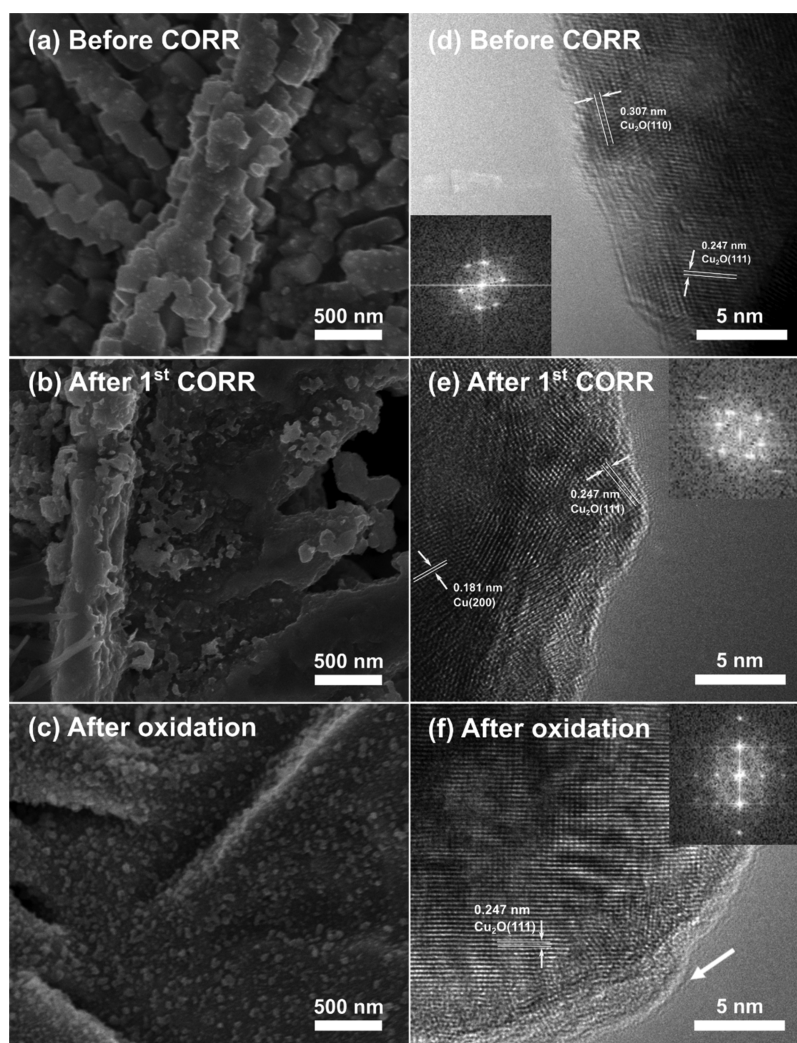
Figure 5. Morphological transformation of Cu-GDE during the CORR. (a−c) SEM and (d−f) TEM images of Cu-GDE before and after electrolysis and subsequent electrochemical oxidation: (a and d) as-synthesized Cu-GDE before the CORR, (b and e) after first the CORR under −2.2 V versus Ag/AgCl taken at 60 min, (c and f) after applying the anodic potential of 1.5 V versus Ag/AgCl for 5 min. The white arrow indicates an amorphous surface layer on the newly formed nanoparticles after anodic oxidation. The insets of the TEM images indicate representative FFT analysis on a selected area to calculate the local *d*-spacing value.

nanocube showed $Cu_2O(111)$ and (110) phases, but additional CuO phase patterns were also observed due to the surface oxidation in ambient conditions during the *ex situ* TEM analysis (Figure S15). After the initial CORR proceeded for 60 min, the nanocubes were no longer observed, having coalesced into a smooth surface (Figure 5b). The TEM image showed that the crystalline surface was still maintained even after CORR (Figure 5e). This result is in agreement with a degradation mechanism induced by either H- or CO-adsorbates under highly negative potentials.[50] After applying a positive potential of 1.5 V for 5 min, the Cu surfaces became covered with nanoparticles ranging in size from 50 to 80 nm (Figure 5c). The nanoparticles had an amorphous surface structure resulting from anodic oxidation treatment (Figure 5f). As the second period of the CORR proceeded, the newly formed nanoparticles also coalesced into a flat and smooth surface (Figure S16). A similar trend of coalescence during the CORR and subsequent formation of nanoparticles during anodic oxidation was also observed for both Cu_2O- and CuO-GDE (Figure S17), suggesting the generality of this

morphological transformation irrespective of the initial oxidation states and morphology.

This finding suggests a hypothesis regarding the catalyst properties that determine the CORR activity and selectivity in the gas-fed cell. At the early stage of the electrolysis, the lower wetted surface area and larger particle size compared to those after anodic oxidation are likely to hinder the generation of Cu active sites by restricting the morphological transformation of the catalysts. Moreover, the coalescence of nanostructures into smooth surfaces as the CORR proceeds can also limit the availability of active sites during CORR, leading to a decrease of C_2H_4 partial current densities as a function of time in all Cu catalysts. After anodic oxidation, the enhancements of the C_2H_4 activity and selectivity may result from the formation of oxide nanoparticles at the surface and their rapid reduction, which could create a more active Cu structure. A reconstructed Cu structure is consistent with previous studies demonstrating that the electrochemical oxidative−reductive process generates selective active sites for C−C coupling.[43,51] While we cannot rule out a small fraction of the oxidized Cu below the error range of our LCF analysis, these post-mortem measurements

suggest that the control over the morphological transformation during catalysis may be a key parameter for achieving high catalytic activities in a practical CO electrolyzer.

Restoration of Cell Performance by Electrochemical Oxidation. Inspired by the above results, we explored the possibility of restoring the cell performance through an anodic oxidation process. We first measured the gaseous and liquid products before and after oxidation in the gas-fed cell (Figure S17). Remarkably, we note that applying 0.1 V during the oxidative step was enough to enhance the C_2H_4 activity, and only $FE_{C_2H_4}$ was enhanced while the other C_{2+} products were similar after anodic oxidation (Table S3). The C_2H_4 partial current densities rapidly decreased over 30 min after anodic oxidation, suggesting that the active sites are unstable under high reaction rates with large overpotentials. We hypothesize that the anodic oxidation can regenerate the stepped Cu active sites from the sintered Cu surface, making it possible to recover the activity periodically without any cell disassembly. To this end, we operated the gas-fed cell at a fixed potential of −2.2 V for 1 h before applying 0.1 V for 5 min, followed by alternating −2.2 V for 30 min and 0.1 V for 5 min (Figure 6).
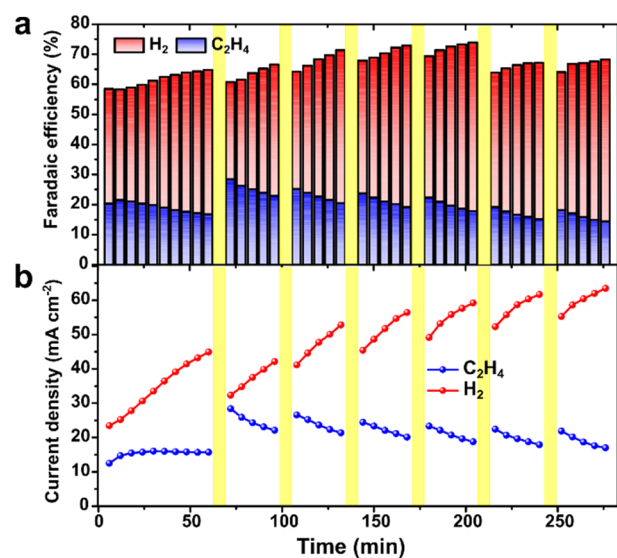

Figure 6. Restoring the cell performance by applying anodic oxidation. (a) Faradaic efficiency and (b) partial current density for H_2 (red) and C_2H_4 (blue) of Cu-GDE as a function of repeated catalyst regeneration. During the catalyst regeneration periods (yellow region), the cell was treated by applying an anodic potential of 0.1 V for 5 min without cell disassembly.

The first anodic oxidation increased the CORR activity (from 15.7 to 28.4 mA cm^{-2}) and selectivity (16.8 to 28.4%) toward C_2H_4 and suppressed H_2 production, while the enhanced performance degraded over 30 min. Subsequent anodic oxidation cycles showed repeated degradation and recovery of the C_2H_4 current density. During this periodic cycling, the initial current density and FE for C_2H_4 were maintained even after 6 h. However, both the current density and FE for H_2 increased over time. Previous studies showed that this was due to electrolyte crossover from the anode chamber, which limited CO transport to the flooded catalyst layer, indicating that water management is important to suppress H_2 production in gas-fed cells.[33,46] To suppress the parasitic HER, strategies for water management include integrating hydrophobic materials (e.g., polytetrafluoroethylene) into the GDL and controlling

the porous structure of both the catalyst layer and the GDL.[34] Compared to the previous studies that include cell disassembly to restore the performance,[52,53] *in situ* regeneration by periodic anodic oxidation can provide a practical strategy to mitigate gas-fed GDE cell degradation.

■ CONCLUSION

In conclusion, the effect of the oxidation state on the CORR activity of oxide-derived Cu catalysts was investigated by using simultaneous *operando* XAS and online GC measurements. Combining data from the XANES fitting and synchronized product analysis, we found that the C_2H_4 activity and selectivity increased as the oxides were reduced to metallic Cu^0. By introducing an electrochemical oxidation process, which improved the CORR performance, we successfully proved that the oxidation states and specific ion species do not correlate with the activity or selectivity of Cu catalysts. Moreover, activities normalized by ECSA revealed that H_2 production was proportional to the ECSA, while the conversion of CO into C_2H_4 was not affected by the ECSA in the gas-fed cell. We also demonstrated that the modification of the cell design to include an X-ray window for the *operando* study could change the reaction environment, which indicates the importance of the performance characterization in the *operando* cell. Post-mortem microscopic investigations of morphological changes suggest that the electrochemical oxidation and its subsequent reduction may generate a more active Cu structure, surpassing the original activity. This electrochemical oxidation−reduction process was utilized as a regeneration method that restored the original catalyst activity and selectivity in the GDE cell without requiring cell disassembly. On the basis of our comprehensive study, we believe that our results motivate the rational design of catalysts for commercial CO reduction systems.

■ EXPERIMENTAL SECTION

Synthesis of Cu Catalysts with Different Oxidation States. Cu was electrodeposited on graphite-based GDLs (denoted as Cu-GDE, Sigracet, 39AA) in an electrolyte containing 0.15 M $CuCl_2·2H_2O$ (99.99%, Alfa Aeasar), 1 M HCl (37% ACS grade, Sigma-Aldrich), and 20% ethanol (Koptek, 200 proof). Preferential deposition of Cu on one side of the GDL was achieved by applying polyimide tape (Kapton) to one side of the GDL and then immersing it in an electrolyte bath. The cell consisted of the GDL as a working electrode, Cu mesh as a counter electrode, and Ag/AgCl (saturated (sat.) KCl) as a reference electrode. Then, −0.5 V versus Ag/AgCl was applied for a total charge of 4.5 C cm^{-2}. After deposition, the resulting Cu-GDE was taken out of the solution and dipped into deionized water several times to rinse the excess electrolyte. After rinsing, the Kapton tape was removed from the backside, and the electrode was dried in air. Cu_2O was also electrodeposited on GDLs (denoted as Cu_2O-GDE, Sigracet, 39AA) in an aqueous electrolyte containing 0.2 M $CuSO_4$ and 3.0 M lactic acid. The pH was adjusted to 12, using a concentrated NaOH solution. Depositions were performed in a 3-electrode configuration using the GDL as a working electrode, Pt coil as a counter electrode, and Ag/AgCl (sat. KCl) as a reference electrode. Then, −0.5 mA cm^{-2} was applied to the working electrode for 1.1 h at 60 °C. The rinsing process was the same as that of Cu-GDE. To fabricate the CuO on the GDL, Cu-GDEs were electrodeposited as above,

followed by oxidation in the air at 350 °C for 16 h in a muffle furnace (denoted as CuO-GDE).

Characterization. A scanning electron microscope (SEM, FEI Inc., NOVA NanoSEM 450) with an integrated energy-dispersive X-ray (EDX) spectrometer was used to analyze the morphology and elemental composition, respectively. Images were taken using an accelerating voltage of 15 kV. EDX images were taken with an accelerating voltage of 15 kV. X-ray diffraction (XRD) measurements were taken with a Bruker D8 Discover X-ray diffractometer using Cu Kα radiation (1.54056 Å) in a Bragg−Brentano geometry. Diffraction images were collected using a two-dimensional VÅNTEC-500 detector and integrated into one-dimensional patterns using DIFFRAC.-SUITE EVA software. Transmission electron microscopy (TEM) was performed using an F20 UT Tecnai (FEI) microscope at an acceleration voltage of 200 kV.

Electrochemical Measurements. Electrochemical measurements were performed using a Biologic SP-300 model potentiostat. The GDE served as a working electrode, Pt mesh as a counter electrode, and Ag/AgCl (sat. KCl) as a reference electrode. The custom GDE cell consisted of two plates that sandwiched the Cu/Cu$_2$O/CuO-GDE, anion exchange membrane (FAA-3-50, Fumatech), and Pt mesh anode and was tightened with external screws. Then, 1.0 M KOH was circulated through the anode chamber, which also contained the reference electrode, as described earlier.[33] All measurements were performed at room temperature (25 °C) and pressure (1 atm). The GDE cell was allowed to equilibrate at OCV conditions until the OCV measured −1.0 V, typically 1 h. EIS measurements were taken at OCV conditions using a range of frequencies of 1 MHz to 0.5 Hz and an amplitude of 10 mV.

Product Analysis. Gas products were measured with online gas chromatography (GC, customized SRI instruments Model 8610C) every 6 min. A thermal conductivity detector (TCD) was used to detect H$_2$, while a flame ionization detector (FID) was used to detect CH$_4$, C$_2$H$_4$, and C$_2$H$_6$ products. A parallel column configuration was employed using a molecular sieve with a 5 Å column for H$_2$, O$_2$, N$_2$, and CO separation and a Haysep D column to separate CH$_4$, CO, CO$_2$, C$_2$H$_4$, and C$_2$H$_6$. An isothermal method was used with an oven temperature of 110 °C, a TCD temperature of 105 °C, a FID temperature of 100 °C, and an injection valve of 60 °C. The Ar carrier gas was set to 20 psi, H$_2$ methanizer gas set to 20 psi, and air pump set to 5 psi. Liquid products were analyzed from the anode side of the cell with high-performance liquid chromatography (HPLC, Dionex UltiMate 3000). The eluent was 1 mM H$_2$SO$_4$ in water with a flow rate of 0.6 mL min^{-1} and a column pressure of 76 bar. The column was an Aminex HPX 87-H from Biorad, held at 60 °C with an internal heater. The detector was a UV detector set to 250 nm. The injection volume was 10 μL. For the determination of liquid products over time, 0.5 mL of anolyte was taken from the anolyte reservoir every 6 min, in conjunction with GC measurements. The faradaic efficiency (FE) was calculated as follows: FE = $e \times F \times n/Q = e \times F \times n/(I \times t)$, where e is the number of electrons transferred, F is the Faraday constant, Q is the charge, I is current, t is the running time, and n is the total amount of product (in moles).

***Operando* X-ray Absorption Spectroscopy and Data Analysis.** *Operando* X-ray absorption spectroscopy (XAS) measurements were conducted at the Stanford Synchrotron Radiation Lightsource (SSRL) on beamline 7-3 at the Cu K edge. The *operando* experiments were performed under CO gas conditions using a GDE cell setup identical to the one used for evaluating the CORR,[33] with a slight modification of a polyimide (Kapton) window to allow for X-ray penetration on the vapor side and with the cell positioned at 45° from the incident X-ray beam. The X-ray energy was tuned by a Si (220) double-crystal monochromator, and the intensity of the incident X-rays (I_0) was monitored by an Ar-filled ion chamber in front of the GDE cell. Data were collected as fluorescence excitation spectra at room temperature using a Ge 30 element detector (Canberra). The data analysis of the Cu K edge X-ray absorption near-edge spectroscopy (XANES) and extended X-ray absorption fine structure (EXAFS) spectra was performed using the Athena software package.[54] Pre-edge and post-edge backgrounds were subtracted from the XAS spectra, and the resulting spectra were normalized by the edge height. For the EXAFS spectra, three consecutive scans were averaged to increase the signal-to-noise ratio, and data reduction was performed with Athena software. The procedures used for the overabsorption correction and linear combination fitting (LCF) analysis are described in detail in Supporting Information.

Electrochemical Oxidation. Potentiostatic electrochemical oxidation of the GDE films was performed by applying 1.5 or 0.1 V for 5 min after bulk electrolysis (−2.2 V, 1 h). After 5 min of oxidation, the cell was allowed to equilibrate at OCV for 1 min, followed by second bulk electrolysis at −2.2 V. Cyclic voltammetry (CV) was performed from −1.1 to 0.5 V at a scan rate of 50 mV s^{-1} for 20 cycles, with the scan ending at 0.5 V.

Electrochemical Active Surface Area (ECSA) Measurements. The electrochemically active surface area (ECSA) was determined from the double-layer capacitance of the films in a non-faradaic potential range, typically ±50 mV of the open-circuit voltage (OCV). CV scans were performed at scan rates of 10, 20, 50, 100, and 200 mV s^{-1}, with the potential held at each vertex for 10 s before the next scan. The double-layer capacitance (C_{dl}) is given by the following equation:

$$i_c = \nu C_{dl}$$

where i_c is the charging current (mA) and ν is the scan rate (V s^{-1}). The charging current was plotted as a function of the scan rate, with the slope equal to C_{dl}. The ECSA was then calculated using the following equation:

$$\text{ECSA} = \frac{C_{dl}}{C_s}$$

where C_s is the electrolyte-dependent solution capacitance. We chose to assume a C_s value of 0.04 mF cm^{-2}, as previously described.[55]

■ ASSOCIATED CONTENT

ⓢ Supporting Information

The Supporting Information is available free of charge at https://pubs.acs.org/doi/10.1021/acscatal.0c01670.

> Sample characterizations (XRD), electrochemical measurements (electroactive surface area, faradaic efficiencies for all products), and XAS analyses are provided (PDF)

■ AUTHOR INFORMATION

Corresponding Authors

Walter S. Drisdell − *Joint Center for Artificial Photosynthesis and Chemical Sciences Division, Lawrence Berkeley National Laboratory, Berkeley, California 94720, United States;* ● orcid.org/0000-0002-8693-4562; Email: wsdrisdell@lbl.gov

Chengxiang Xiang − *Joint Center for Artificial Photosynthesis and Division of Chemistry and Chemical Engineering, California Institute of Technology, Pasadena, California 91125, United States;* ● orcid.org/0000-0002-1698-6754; Email: cxx@caltech.edu

Authors

Soo Hong Lee − *Joint Center for Artificial Photosynthesis and Chemical Sciences Division, Lawrence Berkeley National Laboratory, Berkeley, California 94720, United States;* ● orcid.org/0000-0002-2734-9654

Ian Sullivan − *Joint Center for Artificial Photosynthesis and Division of Chemistry and Chemical Engineering, California Institute of Technology, Pasadena, California 91125, United States;* ● orcid.org/0000-0003-0632-4607

David M. Larson − *Joint Center for Artificial Photosynthesis and Chemical Sciences Division, Lawrence Berkeley National Laboratory, Berkeley, California 94720, United States*

Guiji Liu − *Joint Center for Artificial Photosynthesis and Chemical Sciences Division, Lawrence Berkeley National Laboratory, Berkeley, California 94720, United States*

Francesca M. Toma − *Joint Center for Artificial Photosynthesis and Chemical Sciences Division, Lawrence Berkeley National Laboratory, Berkeley, California 94720, United States;* ● orcid.org/0000-0003-2332-0798

Complete contact information is available at:
https://pubs.acs.org/10.1021/acscatal.0c01670

Author Contributions

[#]S.H.L. and I.S. contributed equally to this work.

Notes

The authors declare no competing financial interest.

■ REFERENCES

(1) De Luna, P.; Hahn, C.; Higgins, D.; Jaffer, S. A.; Jaramillo, T. F.; Sargent, E. H. What would it take for renewably powered electrosynthesis to displace petrochemical processes? *Science* **2019**, *364*, No. eaav3506.

(2) Singh, M. R.; Bell, A. T. Design of an artificial photosynthetic system for production of alcohols in high concentration from CO_2. *Energy Environ. Sci.* **2016**, *9*, 193−199.

(3) Francis, S. A.; Velazquez, J. M.; Ferrer, I. M.; Torelli, D. A.; Guevarra, D.; McDowell, M. T.; Sun, K.; Zhou, X.; Saadi, F. H.; John, J.; Richter, M. H.; Hyler, F. P.; Papadantonakis, K. M.; Brunschwig, B. S.; Lewis, N. S. Reduction of Aqueous CO_2 to 1-Propanol at MoS_2 Electrodes. *Chem. Mater.* **2018**, *30*, 4902−4908.

(4) Ross, M. B.; De Luna, P.; Li, Y.; Dinh, C.-T.; Kim, D.; Yang, P.; Sargent, E. H. Designing materials for electrochemical carbon dioxide recycling. *Nat. Catal.* **2019**, *2*, 648−658.

(5) Lum, Y.; Ager, J. W. Sequential catalysis controls selectivity in electrochemical CO_2 reduction on Cu. *Energy Environ. Sci.* **2018**, *11* (10), 2935−2944.

(6) Han, L.; Zhou, W.; Xiang, C. High-Rate Electrochemical Reduction of Carbon Monoxide to Ethylene Using Cu-Nanoparticle-Based Gas Diffusion Electrodes. *ACS Energy Lett.* **2018**, *3* (4), 855−860.

(7) Zhou, X.; Xiang, C. Comparative Analysis of Solar-to-Fuel Conversion Efficiency: A Direct, One-Step Electrochemical CO2 Reduction Reactor versus a Two-Step, Cascade Electrochemical CO_2 Reduction Reactor. *ACS Energy Lett.* **2018**, *3* (8), 1892−1897.

(8) Hori, Y.; Takahashi, R.; Yoshinami, Y.; Murata, A. Electrochemical Reduction of CO at a Copper Electrode. *J. Phys. Chem. B* **1997**, *101*, 7075−7081.

(9) Peterson, A. A.; Abild-Pedersen, F.; Studt, F.; Rossmeisl, J.; Nørskov, J. K. How copper catalyzes the electroreduction of carbon dioxide into hydrocarbon fuels. *Energy Environ. Sci.* **2010**, *3*, 1311−1315.

(10) Hoang, T. T. H.; Verma, S.; Ma, S.; Fister, T. T.; Timoshenko, J.; Frenkel, A. I.; Kenis, P. J. A.; Gewirth, A. A. Nanoporous Copper−Silver Alloys by Additive-Controlled Electrodeposition for the Selective Electroreduction of CO_2 to Ethylene and Ethanol. *J. Am. Chem. Soc.* **2018**, *140*, 5791−5797.

(11) Wang, L.; Nitopi, S.; Wong, A. B.; Snider, J. L.; Nielander, A. C.; Morales-Guio, C. G.; Orazov, M.; Higgins, D. C.; Hahn, C.; Jaramillo, T. F. Electrochemically converting carbon monoxide to liquid fuels by directing selectivity with electrode surface area. *Nat. Catal.* **2019**, *2*, 702−708.

(12) Ma, S.; Sadakiyo, M.; Heima, M.; Luo, R.; Haasch, R. T.; Gold, J. I.; Yamauchi, M.; Kenis, P. J. A. Electroreduction of Carbon Dioxide to Hydrocarbons Using Bimetallic Cu−Pd Catalysts with Different Mixing Patterns. *J. Am. Chem. Soc.* **2017**, *139*, 47−50.

(13) Perryman, J. T.; Ortiz-Rodríguez, J. C.; Jude, J. W.; Hyler, F. P.; Davis, R. C.; Mehta, A.; Kulkarni, A. R.; Patridge, C. J.; Velázquez, J. M. Metal-promoted Mo_6S_8 clusters: a platform for probing ensemble effects on the electrochemical conversion of CO_2 and CO to methanol. *Mater. Horiz.* **2020**, *7*, 193−202.

(14) Li, C. W.; Ciston, J.; Kanan, M. W. Electroreduction of carbon monoxide to liquid fuel on oxide-derived nanocrystalline copper. *Nature* **2014**, *508*, 504−507.

(15) Verdaguer-Casadevall, A.; Li, C. W.; Johansson, T. P.; Scott, S. B.; McKeown, J. T.; Kumar, M.; Stephens, I. E. L.; Kanan, M. W.; Chorkendorff, I. Probing the Active Surface Sites for CO Reduction on Oxide-Derived Copper Electrocatalysts. *J. Am. Chem. Soc.* **2015**, *137*, 9808−9811.

(16) Jiang, K.; Huang, Y.; Zeng, G.; Toma, F. M.; Goddard, W. A.; Bell, A. T. Production of C_2/C_3 Oxygenates from Planar Copper Nitride-Derived Mesoporous Copper via Electrochemical Reduction of CO_2. *ACS Energy Lett.* **2020**, *5* (4), 1206−1214.

(17) Lum, Y.; Ager, J. W. Stability of Residual Oxides in Oxide-Derived Copper Catalysts for Electrochemical CO_2 Reduction Investigated with [18]O Labeling. *Angew. Chem., Int. Ed.* **2018**, *57*, 551−554.

(18) Lum, Y.; Yue, B.; Lobaccaro, P.; Bell, A. T.; Ager, J. W. Optimizing C−C Coupling on Oxide-Derived Copper Catalysts for Electrochemical CO_2 Reduction. *J. Phys. Chem. C* **2017**, *121*, 14191−14203.

(19) Feng, X.; Jiang, K.; Fan, S.; Kanan, M. W. A Direct Grain-Boundary-Activity Correlation for CO Electroreduction on Cu Nanoparticles. *ACS Cent. Sci.* **2016**, *2*, 169−174.

(20) Mariano, R. G.; McKelvey, K.; White, H. S.; Kanan, M. W. Selective increase in CO_2 electroreduction activity at grain-boundary surface terminations. *Science* **2017**, *358*, 1187−1192.

(21) Xiao, H.; Goddard, W. A.; Cheng, T.; Liu, Y. Cu metal embedded in oxidized matrix catalyst to promote CO_2 activation and CO dimerization for electrochemical reduction of CO_2. *Proc. Natl. Acad. Sci. U. S. A.* **2017**, *114* (26), 6685−6688.

(22) Favaro, M.; Xiao, H.; Cheng, T.; Goddard, W. A.; Yano, J.; Crumlin, E. J. Subsurface oxide plays a critical role in CO_2 activation by Cu(111) surfaces to form chemisorbed CO_2, the first step in reduction of CO_2. *Proc. Natl. Acad. Sci. U. S. A.* **2017**, *114* (26), 6706−6711.

(23) Eilert, A.; Cavalca, F.; Roberts, F. S.; Osterwalder, J.; Liu, C.; Favaro, M.; Crumlin, E. J.; Ogasawara, H.; Friebel, D.; Pettersson, L. G. M.; Nilsson, A. Subsurface Oxygen in Oxide-Derived Copper Electrocatalysts for Carbon Dioxide Reduction. *J. Phys. Chem. Lett.* **2017**, *8*, 285−290.

(24) Mistry, H.; Varela, A. S.; Bonifacio, C. S.; Zegkinoglou, I.; Sinev, I.; Choi, Y.-W.; Kisslinger, K.; Stach, E. A.; Yang, J. C.; Strasser, P.; Cuenya, B. R. Highly selective plasma-activated copper catalysts for carbon dioxide reduction to ethylene. *Nat. Commun.* **2016**, *7* (1), 12123.

(25) Gao, D.; Zegkinoglou, I.; Divins, N. J.; Scholten, F.; Sinev, I.; Grosse, P.; Roldan Cuenya, B. Plasma-Activated Copper Nanocube Catalysts for Efficient Carbon Dioxide Electroreduction to Hydrocarbons and Alcohols. *ACS Nano* **2017**, *11*, 4825−4831.

(26) Chan, C. K.; Tüysüz, H.; Braun, A.; Ranjan, C.; La Mantia, F.; Miller, B. K.; Zhang, L.; Crozier, P. A.; Haber, J. A.; Gregoire, J. M.; Park, H. S.; Batchellor, A. S.; Trotochaud, L.; Boettcher, S. W. Advanced and In Situ Analytical Methods for Solar Fuel Materials. In *Solar Energy for Fuels*; Tüysüz, H., Chan, C. K., Eds.; Springer International Publishing: Cham, Switzerland, 2016; pp 253−324.

(27) De Luna, P.; Quintero-Bermudez, R.; Dinh, C.-T.; Ross, M. B.; Bushuyev, O. S.; Todorović, P.; Regier, T.; Kelley, S. O.; Yang, P.; Sargent, E. H. Catalyst electro-redeposition controls morphology and oxidation state for selective carbon dioxide reduction. *Nat. Catal.* **2018**, *1*, 103−110.

(28) Jouny, M.; Luc, W.; Jiao, F. High-rate electroreduction of carbon monoxide to multi-carbon products. *Nat. Catal.* **2018**, *1*, 748−755.

(29) Burdyny, T.; Smith, W. A. CO_2 reduction on gas-diffusion electrodes and why catalytic performance must be assessed at commercially-relevant conditions. *Energy Environ. Sci.* **2019**, *12*, 1442−1453.

(30) Li, J.; Che, F.; Pang, Y.; Zou, C.; Howe, J. Y.; Burdyny, T.; Edwards, J. P.; Wang, Y.; Li, F.; Wang, Z.; De Luna, P.; Dinh, C.-T.; Zhuang, T.-T.; Saidaminov, M. I.; Cheng, S.; Wu, T.; Finfrock, Y. Z.; Ma, L.; Hsieh, S.-H.; Liu, Y.-S.; Botton, G. A.; Pong, W.-F.; Du, X.; Guo, J.; Sham, T.-K.; Sargent, E. H.; Sinton, D. Copper adparticle enabled selective electrosynthesis of n-propanol. *Nat. Commun.* **2018**, *9* (1), 4614.

(31) Kondrat, S. A.; van Bokhoven, J. A. A Perspective on Counting Catalytic Active Sites and Rates of Reaction Using X-Ray Spectroscopy. *Top. Catal.* **2019**, *62*, 1218−1227.

(32) Newton, M. A.; Knorpp, A. J.; Pinar, A. B.; Sushkevich, V. L.; Palagin, D.; van Bokhoven, J. A. On the Mechanism Underlying the Direct Conversion of Methane to Methanol by Copper Hosted in Zeolites; Braiding Cu K-Edge XANES and Reactivity Studies. *J. Am. Chem. Soc.* **2018**, *140*, 10090−10093.

(33) Sullivan, I.; Han, L.; Lee, S. H.; Lin, M.; Larson, D. M.; Drisdell, W. S.; Xiang, C. A Hybrid Catalyst-Bonded Membrane Device for Electrochemical Carbon Monoxide Reduction at Different Relative Humidities. *ACS Sustainable Chem. Eng.* **2019**, *7*, 16964−16970.

(34) Li, H.; Tang, Y.; Wang, Z.; Shi, Z.; Wu, S.; Song, D.; Zhang, J.; Fatih, K.; Zhang, J.; Wang, H.; Liu, Z.; Abouatallah, R.; Mazza, A. A review of water flooding issues in the proton exchange membrane fuel cell. *J. Power Sources* **2008**, *178*, 103−117.

(35) Manceau, A.; Marcus, M. A.; Grangeon, S. Determination of Mn valence states in mixed-valent manganates by XANES spectroscopy. *Am. Mineral.* **2012**, *97*, 816−827.

(36) Manceau, A.; Marcus, M. A.; Tamura, N. Quantitative Speciation of Heavy Metals in Soils and Sediments by Synchrotron X-ray Techniques. *Rev. Mineral. Geochem.* **2002**, *49*, 341−428.

(37) Pang, Y.; Li, J.; Wang, Z.; Tan, C.-S.; Hsieh, P.-L.; Zhuang, T.-T.; Liang, Z.-Q.; Zou, C.; Wang, X.; De Luna, P.; Edwards, J. P.; Xu, Y.; Li, F.; Dinh, C.-T.; Zhong, M.; Lou, Y.; Wu, D.; Chen, L.-J.; Sargent, E. H.; Sinton, D. Efficient electrocatalytic conversion of carbon monoxide to propanol using fragmented copper. *Nat. Catal.* **2019**, *2*, 251−258.

(38) Roberts, F. S.; Kuhl, K. P.; Nilsson, A. High Selectivity for Ethylene from Carbon Dioxide Reduction over Copper Nanocube Electrocatalysts. *Angew. Chem., Int. Ed.* **2015**, *54*, 5179−5182.

(39) Ren, D.; Deng, Y.; Handoko, A. D.; Chen, C. S.; Malkhandi, S.; Yeo, B. S. Selective Electrochemical Reduction of Carbon Dioxide to Ethylene and Ethanol on Copper(I) Oxide Catalysts. *ACS Catal.* **2015**, *5*, 2814−2821.

(40) Strehblow, H.-H.; Maurice, V.; Marcus, P. Initial and later stages of anodic oxide formation on Cu, chemical aspects, structure and electronic properties. *Electrochim. Acta* **2001**, *46*, 3755−3766.

(41) Gao, D.; Sinev, I.; Scholten, F.; Arán-Ais, R. M.; Divins, N. J.; Kvashnina, K.; Timoshenko, J.; Roldan Cuenya, B. Selective CO_2 Electroreduction to Ethylene and Multicarbon Alcohols via Electrolyte-Driven Nanostructuring. *Angew. Chem., Int. Ed.* **2019**, *58*, 17047−17053.

(42) Zhou, Y.; Che, F.; Liu, M.; Zou, C.; Liang, Z.; De Luna, P.; Yuan, H.; Li, J.; Wang, Z.; Xie, H.; Li, H.; Chen, P.; Bladt, E.; Quintero-Bermudez, R.; Sham, T.-K.; Bals, S.; Hofkens, J.; Sinton, D.; Chen, G.; Sargent, E. H. Dopant-induced electron localization drives CO_2 reduction to C_2 hydrocarbons. *Nat. Chem.* **2018**, *10*, 974−980.

(43) Baricuatro, J. H.; Kim, Y.-G.; Tsang, C. F.; Javier, A. C.; Cummins, K. D.; Hemminger, J. C. Selective conversion of CO into ethanol on Cu(511) surface reconstructed from Cu(pc): *Operando* studies by electrochemical scanning tunneling microscopy, mass spectrometry, quartz crystal nanobalance, and infrared spectroscopy. *J. Electroanal. Chem.* **2020**, *857*, 113704.

(44) Wang, L.; Nitopi, S. A.; Bertheussen, E.; Orazov, M.; Morales-Guio, C. G.; Liu, X.; Higgins, D. C.; Chan, K.; Nørskov, J. K.; Hahn, C.; Jaramillo, T. F. Electrochemical Carbon Monoxide Reduction on Polycrystalline Copper: Effects of Potential, Pressure, and pH on Selectivity toward Multicarbon and Oxygenated Products. *ACS Catal.* **2018**, *8*, 7445−7454.

(45) Clark, E. L.; Resasco, J.; Landers, A.; Lin, J.; Chung, L.-T.; Walton, A.; Hahn, C.; Jaramillo, T. F.; Bell, A. T. Standards and Protocols for Data Acquisition and Reporting for Studies of the Electrochemical Reduction of Carbon Dioxide. *ACS Catal.* **2018**, *8*, 6560−6570.

(46) Leonard, M.; Clarke, L. E.; Forner-Cuenca, A.; Brown, S. M.; Brushett, F. Investigating Electrode Flooding in a Flowing Electrolyte, Gas-Fed Carbon Dioxide Electrolyzer. *ChemSusChem* **2020**, *13*, 400−411.

(47) Santamaria, A. D.; Das, P. K.; MacDonald, J. C.; Weber, A. Z. Liquid-Water Interactions with Gas-Diffusion Layer. *J. Electrochem. Soc.* **2014**, *161* (12), F1184−F1193.

(48) Eren, B.; Zherebetskyy, D.; Patera, L. L.; Wu, C. H.; Bluhm, H.; Africh, C.; Wang, L.-W.; Somorjai, G. A.; Salmeron, M. Activation of Cu(111) surface by decomposition into nanoclusters driven by CO adsorption. *Science* **2016**, *351*, 475−478.

(49) Kim, Y.-G.; Baricuatro, J. H.; Javier, A.; Gregoire, J. M.; Soriaga, M. P. The Evolution of the Polycrystalline Copper Surface, First to Cu(111) and Then to Cu(100), at a Fixed CO_2RR Potential: A Study by Operando EC-STM. *Langmuir* **2014**, *30*, 15053−15056.

(50) Huang, J.; Hörmann, N.; Oveisi, E.; Loiudice, A.; De Gregorio, G. L.; Andreussi, O.; Marzari, N.; Buonsanti, R. Potential-induced nanoclustering of metallic catalysts during electrochemical CO_2 reduction. *Nat. Commun.* **2018**, *9* (1), 3117.

(51) Kim, Y.-G.; Javier, A.; Baricuatro, J. H.; Soriaga, M. P. Regulating the Product Distribution of CO Reduction by the Atomic-Level Structural Modification of the Cu Electrode Surface. *Electrocatalysis* **2016**, *7*, 391−399.

(52) Endrődi, B.; Kecsenovity, E.; Samu, A.; Darvas, F.; Jones, R. V.; Török, V.; Danyi, A.; Janáky, C. Multilayer Electrolyzer Stack Converts Carbon Dioxide to Gas Products at High Pressure with High Efficiency. *ACS Energy Lett.* **2019**, *4*, 1770−1777.

(53) Gurudayal; Beeman, J. W.; Bullock, J.; Wang, H.; Eichhorn, J.; Towle, C.; Javey, A.; Toma, F. M.; Mathews, N.; Ager, J. W. Si photocathode with Ag-supported dendritic Cu catalyst for CO_2 reduction. *Energy Environ. Sci.* **2019**, *12*, 1068−1077.

(54) Ravel, B.; Newville, M. ATHENA, ARTEMIS, HEPHAESTUS: data analysis for X-ray absorption spectroscopy using IFEFFIT. *J. Synchrotron Radiat.* **2005**, *12*, 537−541.

(55) McCrory, C. C. L.; Jung, S.; Peters, J. C.; Jaramillo, T. F. Benchmarking Heterogeneous Electrocatalysts for the Oxygen Evolution Reaction. *J. Am. Chem. Soc.* **2013**, *135*, 16977−16987.